RSC Advances

ROYAL SOCIETY OF CHEMISTRY

www.rsc.org/advances

Cite this: DOI: 10.1039/c0xx00000x

www.rsc.org/xxxxxx

ARTICLE TYPE

One-pot synthesis of heterostructured Bi_2S_3/BiOBr microspheres with highly efficient visible light photocatalytic performance

Hong-Peng Jiao[a], Xiang Yu[a], Zhao-Qing Liu*[b], Pan-Yong Kuang[b], and Yuan-Ming Zhang*[a]

Received (in XXX, XXX) Xth XXXXXXXXX 20XX, Accepted Xth XXXXXXXXX 20XX

DOI: 10.1039/b000000x

To overcome the drawback of low photocatalytic efficiency brought by fast electron-hole recombination and narrow photoresponse range, the heterostructured Bi_2S_3/BiOBr microspheres were designed and synthesized *via* a facile one-pot solvothermal method. The as-prepared heterostructured Bi_2S_3/BiOBr photocatalyst exhibits significantly enhanced photoelectrochemical performance and photocatalytic activity for decomposing rhodamine B (RhB) and Brilliant ponceau 5R (BP) compared with pure BiOBr under visible light irradiation, which could be mainly attributed to the formation of heterojunction in the Bi_2S_3/BiOBr interface, which can efficiently facilitate the separation of photogenerated electron-hole pairs. Furthermore, terephthalic acid photoluminescence (TA-PL) probing test and radical trapping experiments demonstrate that the h^+ and $•O^{2-}$ radicals are the dominant reactive species while •OH radicals could be neglected. In addition, the possible enhanced photocatalytic mechanism is proposed on the basis of the calculated energy band positions and radical trapping experiments.

1. Introduction

Recent years, semiconductor photocatalysts have drawn more and more attention due to their widespread application in environmental pollutant remediation[1-3] as well as solar energy conversion and storage[4-6]. Nevertheless, the conventional photocatalytic semiconductor materials, such as TiO_2 and ZnO, suffered from the limitation of ultraviolet light absorption, which accounts for less than 5% of natural light.[7-10] For purpose of efficient utilization of solar energy, the exploration of new type visible light responsed photocatalysts with high catalytic performance has become one of the most pivotal topics in contemporary photocatalysis research.

As a class of layered semiconductors, bismuth oxyhalides BiOX (X = Cl, Br, I) with unique tetragonal structure, are evoking great interests due to their excellent photocatalytic activity under both ultraviolet and visible-light illumination.[11-13] In particular, the layered structure of BiOX[14,15] consisting of tetragonal $[Bi_2O_2]^{2+}$ positive slabs interleaved by double negative slabs of halogen atoms along the *c* axis, which provides the space large enough to polarize the related atoms and orbits. Furthermore, the induced dipole can efficiently separate the electron-hole pairs, leading to the superior photocatalytic activity. Therefore, it may be an ideal choice to rationally design the efficient BiOX-based visible light photocatalysts. Among them, bismuth oxybromine (BiOBr) is of great research interest for its good chemical stability and relatively superior photocatalytic ability.[16,17] However, the wide band gap (E_g = 2.90 eV) inevitably leading to the weak absorption of visible light. To date, it is still a challenge to improve the visible light response and separation efficiency of photogenerated electron-hole pairs of BiOBr considering its future practical application.

To utilize visible light more efficiently and improve visible light photocatalytic activity of BiOBr, some strategies including controllable synthesis, [18] doping metals,[19,20] and combination with other materials such as graphene,[21] *g*-C_3N_4,[22] TiO_2,[23] $ZnFe_2O_4$,[24] $BiWO_6$[25] and Ag/AgBr[26] have been successfully employed. Worth to be mentioned, the construction of BiOBr-based heterostructured composite is considered as an effective and promising way to promote the photocatalytic performance. Such photocatalysts integrating the synergistic effects of the individual species, which could endow the composite systems with increased visible light harvesting ability, improved separation efficiency of photogenerated electron-hole pairs, and prolonged lifetime of carriers, thereby resulting in the enhanced photocatalytic activity.

As a common metal sulfide, bismuth sulfide (Bi_2S_3) has wide and potential applications in electrochemical hydrogen storage, sensor, thermoelectric devices,[27,28] photovoltaic cells and photoelectrochemical devices[29,30] due to its narrow band gap (E_g = 1.30 eV), large absorption coefficient and reasonable incident photo to electron conversion efficiency. Moreover, the size quantization of Bi_2S_3 exhibits tunable photosensitization and considerable photocatalytic activity in the visible light region. As predicted, enhanced photocatalytic activity has been obtained by combining Bi_2S_3 other semiconductors, such as TiO_2,[31] Fe_3O_4,[32] $BiVO_4$,[33] BiOI[34] and BiOCl.[35] Nevertheless, the related report on the combination of BiOBr and Bi_2S_3 to construct Bi_2S_3/BiOBr

Cite this: DOI: 10.1039/c0xx00000x

www.rsc.org/xxxxxx

ARTICLE TYPE

heterostructure and the investigation of the enhanced photocatalytic mechanism is still very limited.

In this work, a novel hierarchical Bi_2S_3/BiOBr heterostructured composite was synthesized by a facile one-pot solvothermal method for the first time. Bi_2S_3/BiOBr composite was fabricated by controlled release of Br^- and S^{2-} from KBr and thiourea (NH_2CSNH_2) to react with Bi^{3+} and a partial anion exchange reaction. Intimate contact and well defined junction between Bi_2S_3 and BiOBr could be built easily through this route, which could effectively facilitate the transfer efficiency and suppress the recombination rate of photogenerated electron-hole pairs, resulting in extremely high activity and stability. The hierarchical Bi_2S_3/BiOBr heterostructured composite served as a versatile photocatalyst by degrading rhodamine B and Brilliant ponceau 5R under visible light illumination, exhibited superior photocatalytic performance compared with the pure BiOBr and Bi_2S_3, indicating the potential application for solving the current environmental problems.

2. Experimental details

2.1. Materials

Bismuth nitrate pentahydrate ($Bi(NO_3)_3{\cdot}5H_2O$, AR), thiourea (CH_3CSNH_2, AR), rhodamine B (RhB, AR), Brilliant ponceau 5R (BP, AR), and benzoquinone (BQ, AR) were obtained from Aladdin Reagent Co., Ltd. (Shanghai, China). Potassium bromide (KBr, AR), sodium sulfate ($NaSO_4$, AR), absolute ethanol, terephthalic acid (TA, AR), and sodium hydroxide (NaOH, AR) were purchased from Guangzhou Chemical reagent Factory (China). Ammonium oxalate (AO, AR), 2-methoxyethanol, and *tert*-butyl alcohol (TBA, AR) were purchased Tianjin Fuchen Chemical Reagents Factory (China). In addition, TiO_2 powder (Degussa P25) was purchased from Degussa Co. (Frankfurt, Germany). All reagents were used directly for the experiment without any further purification. Distilled water was used throughout this study.

2.2. Preparation of BiOBr and Bi_2S_3/BiOBr composite

The BiOBr sample was prepared by a simple solvothermal method, 1 mM of KBr was dissolved in 2-methoxyethanol solution, then the same stoichiometric amount of $Bi(NO_3)_3{\cdot}5H_2O$ was added. The resulting suspension was constantly stirred for 30 min at room temperature, then transferred into a Teflon-lined autoclave (50 mL capacity) and heated at 120 °C for 12 h. After cooling down to room temperature, the obtained precipitates were washed with distilled water and ethanol several times, and dried at 60 °C for 12 h.

The Bi_2S_3/BiOBr microspheres were prepared by a typical solvothermal method, a mixture of 2.4 mM thiourea and 0.7 mM KBr was dissolved in 30 mL 2-methoxyethanol under constant stirring. Meanwhile, 1mM of $Bi(NO_3)_3{\cdot}5H_2O$ was added to 10 mL 2-methoxyethanol to form a clear solution. After that, the two solutions were mixed together and being stirred for 30 min at room temperature. Then the suspension was transferred into a 50 mL Teflon-lined autoclaveand heated at 120 °C for 12 h. Upon completion of the reaction, the products were filtrated from the solution, washed with distilled water and absolute alcohol several times, and dried at 60 °C for 12h. Additionally, pure Bi_2S_3 was prepared by adding 8 mM of CH_3CSNH_2 to a Bi-based 2-methoxyethanol solution (molar ratio of Bi : S = 1 : 8) and a black Bi_2S_3 precipitate was obtained.

2.3. Characterization

Powder X-ray diffraction (XRD) measurement was conducted on a Bruker, D8 ADVANCE diffractometer with monochromatized Cu Kα radiation (λ = 1.5418 Å). The surface morphology and crystal structure of the as-prepared samples were analyzed by field emission scanning electron microscopy (FE-SEM, Zeiss ULTRA 55) and transmission electron microscopy (TEM, JEOL 2010F). Compositions as well as the chemical state of the samples were characterized by energy-dispersive spectroscopy (EDS, Bruker/Quanta 200) and X-ray photoelectron spectroscopy (XPS, ESCALab250). The photoelectrochemical experiment was measured on an electrochemical system (SP-150, France). The optical properties of the products were measured with a UV-Vis-NIR spectrophotometer (UV, Hitachi UV-3010) and a combined fluorescence lifetime and JASCO FP-6500 type fluorescence spectrometer.

2.4. Photocatalytic activity tests

The photocatalytic activity of the samples was evaluated by degrading of rhodamine B (RhB, a commom cationic dye) and Brilliant ponceau 5R (BP, a common anionic dye) under visible light irradiation using a 150-350 W Xenon lamp with a cut-off filter (λ > 420 nm). The system temperature was maintained at room temperature by circulating water. In each experiment, a suspension of 100 mL RhB or BP with a concentration of 50 mg L^{-1} and 0.1 g of the samples were placed in a reactor under vigorous stirring. Prior to irradiation, the suspension was magnetically stirred in dark for 30 min to ensure the establishment of adsorption/desorption equilibrium of the dye on the catalysts' surface. At a given time intervals, a quantitative solution was collected and centrifuged under magnetic stirring, the absorbance of the solution was analyzed by using a UV-vis spectrophotometer. The removal efficiency of dye was calculated by the following equation:

$$\text{Removal} = \frac{C_t}{C_0} \times 100\% \qquad (1)$$

Cite this: DOI: 10.1039/c0xx00000x

www.rsc.org/xxxxxx

ARTICLE TYPE

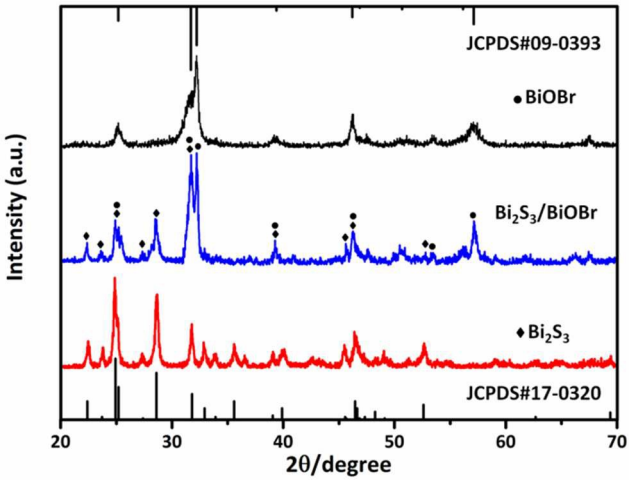

Fig. 1. XRD patterns of the pure Bi_2S_3, the hierarchical heterostructured Bi_2S_3/BiOBr sphere, and the pure BiOBr.

where C_0 is the initial concentration of dye solution, C_t is the reaction concentration at time t.

2.5. Photoelectrochemical Measurements

The photoelectrochemical and electrochemical impedance spectroscopy (EIS) measurements were conducted by using an electrochemical analyzer (SP-150, France) with a standard three-electrode configuration, the Pt wire used as counter electrode, the saturated Ag/AgCl electrode and the as-prepared samples coated on indium tin oxide (ITO) substrate served as reference electrode and working electrode, respectively. For the fabrication of photoanode, the samples were obtained by mixing 1 mL ethanol and 20 mg the as-prepared powder homogeneously. The as-prepared samples were spread on an indium tin oxide (ITO) substrate (2 cm × 4 cm) and allowed to dry under ambient condition. A 150-350 W Xenon lamp with a 420 nm cut-off filter was utilized as the light source. And a 0.2 mol L^{-1} Na_2SO_4 aqueous solution was used as the electrolyte.

2.6. Detection of reactive species

Relevant reactive species were evaluated by adding a quantity of different scavengers in a manner similar to the above photodegradation experiment prior to the addition of the catalyst. The dosages of the scavengers were referred to the previous studies. Terephthalic acid photoluminescence probing technique (TA-PL) was employed to detect •OH radicals, in which a basic TA solution was added to the reactor instead of RhB and the concentration of TA was set at 5×10^{-4} mol L^{-1} in 2×10^{-3} mol L^{-1} NaOH solution. The sample was collected every 10 min and measured on a JASCO FP-6500 type fluorescence spectrophotometer after centrifugation, and the excitation wavelength was 315 nm.

3. Result and discussion

3.1. XRD analysis

The composition and phase structures of the as-prepared samples were examined by X-ray diffraction (XRD). Fig. 1 shows the XRD patterns of the pure Bi_2S_3, BiOBr and Bi_2S_3/BiOBr composite. It can be seen that all the samples are well crystallized and all the diffraction peaks of Bi_2S_3 could be well indexed to the orthorhombic Bi_2S_3 (JCPDS#17-0320), and the feature peaks of the pure BiOBr clearly correspond to the tetragonal phase of BiOBr (JCPDS#09-0393). No impurity peaks are observed, implying that the final products of Bi_2S_3 and BiOBr are of pure phases. The diffraction pattern of Bi_2S_3/BiOBr indicates that the composite is composed of the tetragonal BiOBr and the orthorhombic Bi_2S_3. Therefore, the above results reveal the coexistence of Bi_2S_3 and BiOBr in the Bi_2S_3/BiOBr composite.

3.2. Crystal morphology and microstructure analysis

The morphology of the pure Bi_2S_3, BiOBr, and Bi_2S_3/BiOBr composite were characterized by the field-emission scanning electron microscopy (FE-SEM). It can be seen from the low- and high- magnification pictures (Fig. 2a-c), the pure Bi_2S_3 has a spherical urchin shape, and the diameter is in the range of 2-5 um. The high-magnification SEM image clearly reveals that the individual urchin-like Bi_2S_3 sphere is constructed with radically grown nanorods. By controlling the release of Br^- and S^{2-} from KBr and thiourea (NH_2CSNH_2) to react with Bi^{3+} and a partial anion exchange reaction, the hierarchical Bi_2S_3/BiOBr composite was obtained. From the typical SEM images of the Bi_2S_3/BiOBr composite in Fig. 2d-f, it is observed that the composite contains two different phases. The enlarged images in Fig. 2e-f clearly show that the surface of the urchin-like Bi_2S_3 spheres are stuck with some tiny semi-finished spheres, indicating the intimate contact of Bi_2S_3 and BiOBr. For BiOBr (Fig. 2h-j), the obtained hierarchical spheres are made up of the nanosheets, which are similar with the Bi_2S_3/BiOBr composite in Fig. 2d-f.

The transmission electron microscopy (TEM) observation was performed to further demonstrate the microstructural feature of the pure Bi_2S_3, BiOBr, and hierarchical Bi_2S_3/BiOBr heterostructure. As shown in Fig. 3a-b, the Bi_2S_3 sample is composed of nanorod assembled urchin-like spheres with diameter of about 2-5 μm. Fig. 3c clearly displays a high-resolution transmission electron microscopy (HRTEM) image and the corresponding selected-area electron diffraction (SAED) pattern of a typical Bi_2S_3 nanorod, respectively. The spacing between the two parallel neighboring fringes is 0.79 nm and 0.56 nm, which matches well with the (110) and (020) plane, respectively. The SAED pattern (inset in Fig. 3c) shows a regular spot pattern, confirming the single-crystalline feature of the Bi_2S_3. The morphological feature of the as-prepared hierarchical BiOBr

Cite this: DOI: 10.1039/c0xx00000x

www.rsc.org/xxxxxx

ARTICLE TYPE

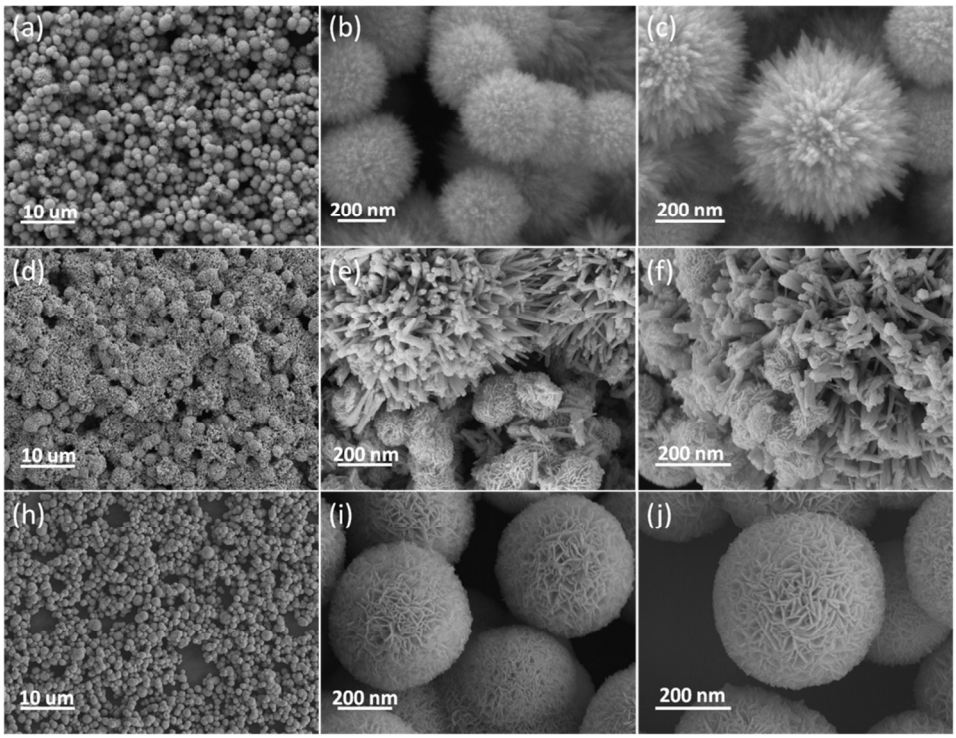

Fig. 2. FE-SEM images of the pure Bi_2S_3 (a-c); the hierarchical heterostructured Bi_2S_3/BiOBr sphere (d-f); and the pure BiOBr (h-j).

spheres is shown in Fig. 3d. It is apparent that the sphere is composed of nanosheet with a size in the range of 50-100 nm. The HRTEM image in Fig. 3e exhibits good crystalline and clear lattice fringes projected along the (001) axis. The continuous lattice fringes with an inter-planar spacing of 0.278 nm and an angle of 90°, which matches well with the (110) atomic plane of the tetragonal BiOBr. As depicted in Fig. 3f, the corresponding SAED pattern displays a spot pattern, indicating the single-crystalline characteristic of the obtained hierarchical spheres. The angle of adjacent spots labeled in the SAED pattern is 45°, which is identical to the theoretical value of the angle between the (110) and (200) planes. Based on the above results and the symmetries of tetragonal BiOBr, the bottom and top surfaces of the BiOBr nanosheets are identified as (001) facets, while the four lateral surfaces are (110) facets (inset in Fig. 3e). Thus, the set of diffraction spots can be indexed as the (001) zone axis of tetragonal BiOBr.

Fig. 4a-b show typical TEM images of the hierarchical heterostructured Bi_2S_3/BiOBr sphere. The border between Bi_2S_3 nanorod and BiOBr nanosheet is nearly invisible, indicating the intimate contact of orthorhombic Bi_2S_3 and BiOBr, as well as the composition fusion which may happen at the interface by ion exchange. Fig. 4c exhibits the HRTEM image of the hierarchical heterostructured Bi_2S_3/BiOBr sphere, the clear lattice fringe with a spacing of 0.79 and 0.37 nm can be matched well with the (110) and (101) plane of orthorhombic Bi_2S_3, respectively. Meanwhile, the fringe spacing of 0.23 nm agrees well with the (112) plane of BiOBr. These phenomenons indicate that the lattice cell of BiOBr could coherently grow on the facets of Bi_2S_3 nanocrystals through a straightforward epitaxial growth process. Therefore, the BiOBr nanosheets are inlaid in the Bi_2S_3 nanorods matrix, not simply ''inserted'' in the Bi_2S_3 nanorods. Interestingly, the Bi_2S_3/BiOBr heterojunctions are formed in the Bi_2S_3/BiOBr composite, which effectively hinders the recombination of photoinduced electron-hole pairs and acquires excellent photocatalytic activities under visible light illumination.[36] To further elucidate microstructure, the EDS elemental full and line mapping techniques were applied to an individual sphere. Fig. 4d-g shows that the elements including Bi, S, Br and O, which are uniformly distributed over the hybrid, demonstrating the nanoscale heterojunction was obtained between Bi_2S_3 and BiOBr architectures.

3.3. Surface composition and metal oxidation states

The X-ray photoelectron spectroscopy (XPS) measurement provides further information for the chemical composition and surface chemical state of the as-prepared hierarchical heterostructured Bi_2S_3/BiOBr sphere. According to the XPS survey spectra in Fig. S1, Br 3d peak around 68.0 eV and S 2s peak around 225.2 eV can be detected for Bi_2S_3/BiOBr sample compared with the pure Bi_2S_3 and BiOBr. Besides Bi, O and Br elements Bi_2S_3/BiOBr contains the S element compared with the BiOBr. Fig. 5a-d show high resolution XPS spectra of the

Cite this: DOI: 10.1039/c0xx00000x

www.rsc.org/xxxxxx

ARTICLE TYPE

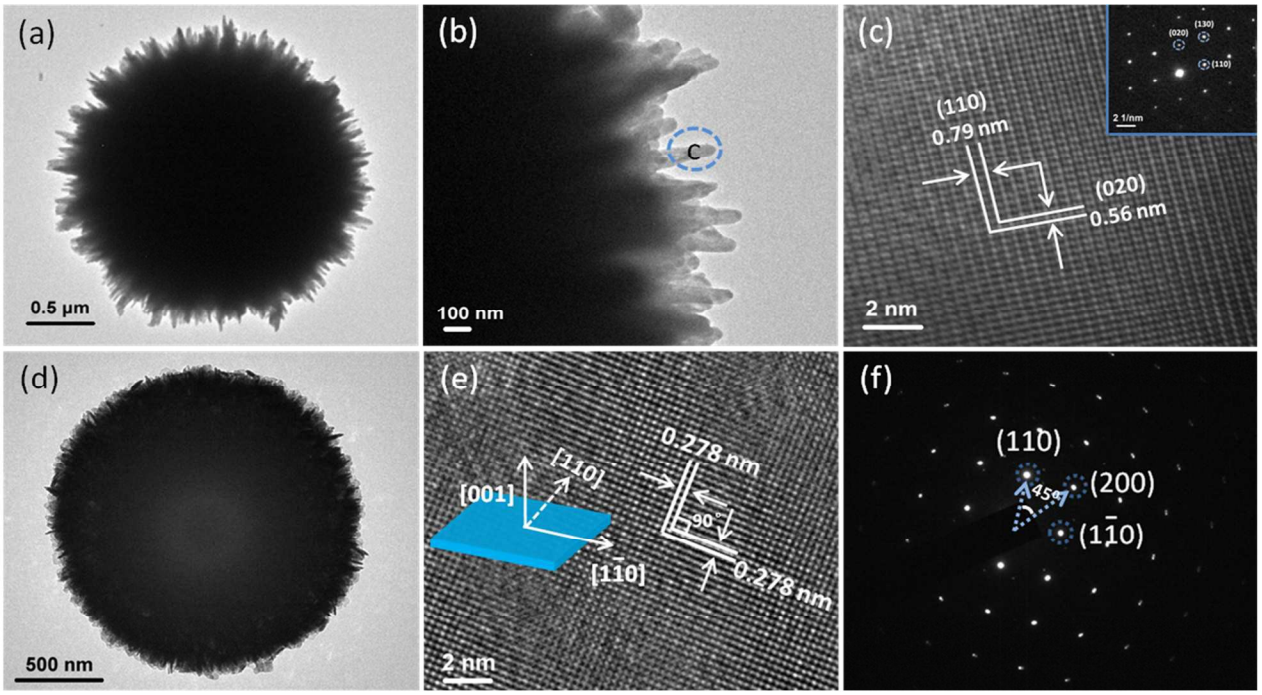

Fig. 3. (a-c) TEM and HRTEM images of urchin-like Bi_2S_3 spheres, the inset is the corresponding SAED pattern; (d-f) TEM, HRTEM and the corresponding SAED pattern of hierarchical BiOBr structure, the inset is the schematic illustration of the crystal orientation of BiOBr.

hierarchical heterostructured Bi_2S_3/BiOBr sphere. As displayed in Fig. 5a, clearly, two strong peaks centered at 163.5 and 158.2 eV can be attributed to the spin orbital splitting photoelectrons of the Bi $4f_{5/2}$ and Bi $4f_{7/2}$, respectively, which is a characteristic of Bi^{3+} in Bi_2S_3 and BiOBr.[37] A slight Bi^{3+} XPS peak shift to low binding energy in Bi_2S_3/BiOBr sample can be observed compared with the BiOBr (Fig. S2a), which may be attribute to the strong chemical bonding between BiOBr and Bi_2S_3.[21,38] The peak (160.9 eV) found between Bi $4f_{7/2}$ and Bi $4f_{5/2}$ could be assigned to S_{2p}.[36] Only one symmetric peak at about 68.2 eV was associated for Br 3d of Bi_2S_3/BiOBr (Fig. 5b) and BiOBr (Fig. S2b), indicating their similar coordination of Br^-.[37] The particular S 2s XPS spectrum can be deconvoluted into two Gaussian peaks (Fig. 5c). The higher energy peak at 225.3 eV is consistent with a Bi-S species.[36] The peak at lower energy observed at 227.1 eV agrees well with the report for the S_8.[39] Meanwhile, the O 1s XPS spectrum of Bi_2S_3/BiOBr (Fig. 5d) and BiOBr (Fig. S2c) can be fitted by two peaks at binding energies of 531.2 and 532.7 eV, respectively, which can be ascribed to the lattice oxygen and other components such as O_2, H_2O or carbonate species adsorbed on the surface of catalysts.[40]

3.4. Nitrogen adsorption-desorption

The enhanced photocatalytic performance of the hierarchical heterostructured Bi_2S_3/BiOBr sphere could be mainly attributed to its excellent physicochemical properties. Fig. 6 presents the N_2 adsorption-desorption isotherms and the corresponding pore-size distribution (PSD) curves of the pure Bi_2S_3, BiOBr, and the hierarchical heterostructured Bi_2S_3/BiOBr sphere. All the curves exhibit the type IV isotherms with a distinct hysteresis loop at the relative pressure P/P_0 ranging from 0.6 to 1.0, which is a characteristic of the mesoporous structure. The BET surface area calculated from the isotherms of the pure Bi_2S_3, BiOBr, and hierarchical heterostructured Bi_2S_3/BiOBr sphere is 8.2, 14.7, and 22.9 m^2g^{-1}, respectively. Notably, the hierarchical heterostructured Bi_2S_3/BiOBr sphere exhibits much higher BET surface area than the pure BiOBr. The significant increase in BET surface area should be ascribed to the aforementioned crystal growth inhibition effect and/or the loose agglomeration between the two components. To further analyze the pore structure of the as-prepared samples, PSD curves have been investigated by using Barrett-Joyner-Halenda (BJH) method. As presented in the inset of Fig. 6, the peak of pore size of the pure Bi_2S_3, BiOBr, and hierarchical heterostructured Bi_2S_3/BiOBr sphere is centered at 10.0, 8.6, and 13.3 nm, respectively. The pores can serve as the path for transfer and distribution of photo energy onto the inner surfaces of porous frameworks, inducing the significant increase of light-activated area due to the multiple reflections of light within the interior cavity. Such multiple reflections can facilitate the photoabsorption efficiency of the catalyst, thus improve the photocatalytic activity. Meanwhile, hierarchical heterostructured Bi_2S_3/BiOBr sphere owns the higher pore volume (0.0761 cm^3/g), compared with pure BiOBr (0.0580 cm^3/g) and Bi_2S_3 (0.0312 cm^3/g), which is beneficial for the adsorption of compounds and

Cite this: DOI: 10.1039/c0xx00000x

www.rsc.org/xxxxxx

ARTICLE TYPE

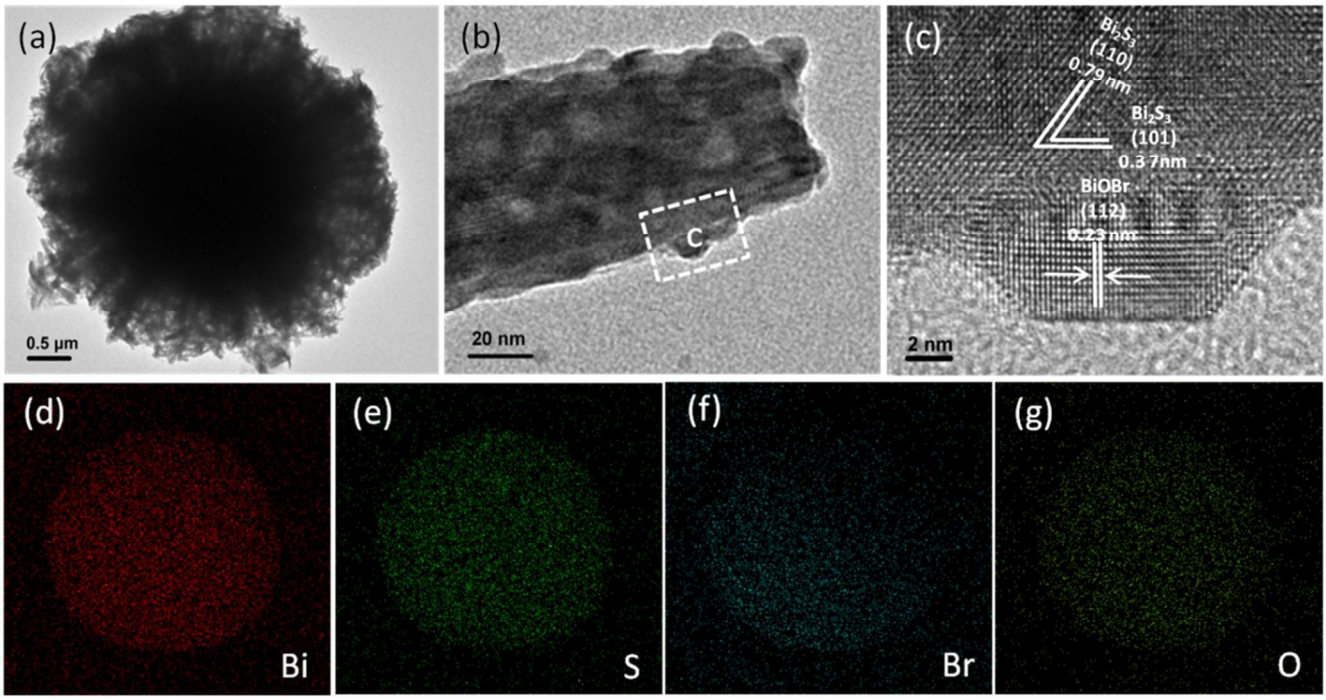

Fig. 4. (a-c) TEM and HRTEM images of Bi_2S_3/BiOBr heterostructures; (d-g) EDX elemental mapping images of the Bi, S, Br, and O, respectively.

transmittance of light during photocatalytic reaction.

3.5. Optical absorption behaviour

It is well known that the optical absorption of photocatalyst and the migration of photoinduced electrons and holes in the photocatalytic reaction are the key factors, which are relevant to the electronic structure characteristics of the material. Thus, UV-vis diffuse reflectance spectroscopy (DRS) was used to detect the photoabsorption ability of the samples. Fig. 7 depicts the diffuse reflectance absorption spectra of the pure Bi_2S_3, BiOBr and the hierarchical heterostructured Bi_2S_3/BiOBr sphere, respectively. Obviously, the pure BiOBr only has weak absorption in visible light region with an absorption edge around 434 nm while the pure Bi_2S_3 shows intense absorption over the visible range even extending to the infrared region. However, the absorption edge of the Bi_2S_3/BiOBr sphere shows a red shift to about 510 nm due to the strong visible light response of Bi_2S_3. The result is consistent with the colour of the samples (the inset in Fig. 7). The results suggest that such Bi_2S_3/BiOBr sphere has enhanced visible light response compared with the pure BiOBr. Therefore, the unusual photocatalytic activity could be expected from the heterojunctions under visible light irradiation assuming the intimate contact interfaces are generated.

Moreover, the optical absorption property of the photocatalyst is often closely associated with its optical energy gap. The band gap energies of the as-prepared samples were calculated by the formula: [41]

$$ahv = A\,(hv - E_g)^{n/2} \qquad (2)$$

where a, h, v, A, E_g, and n is the absorption coefficient, Planck's constant, incident light frequency, constant, the band-gap energy and an integer, respectively. Among them, n depends on the characteristic of the optical transition in a semiconductor, i.e., direct transition (n = 1) and indirect transition (n = 4). For Bi_2S_3 and BiOBr, they pertain to direct and indirect transition, respectively. The E_g of Bi_2S_3 and BiOBr can be estimated from the plot of $(ahv)^2$ versus hv and $(ahv)^{1/2}$ versus hv, respectively. The intercept of the tangent to the x axis will give a good approximation of the band-gap energy for the as-prepared hierarchical Bi_2S_3 and BiOBr microspheres. As shown in Fig. S3, the E_g of the pure Bi_2S_3, and BiOBr are calculated to be 1.30 eV,[42] and 2.85 eV,[41, 43] respectively. They are all less than that of TiO_2 (about 3.2 eV).

3.6. Photocatalytic performance

To demonstrate the potential application of the hierarchical heterostructured Bi_2S_3/BiOBr sphere in the degradation of organic contaminants, we investigated the photocatalytic activities by choosing the photocatalytic degradation of RhB with high concentration as a model reaction. For the purpose of

Cite this: DOI: 10.1039/c0xx00000x

www.rsc.org/xxxxxx

ARTICLE TYPE

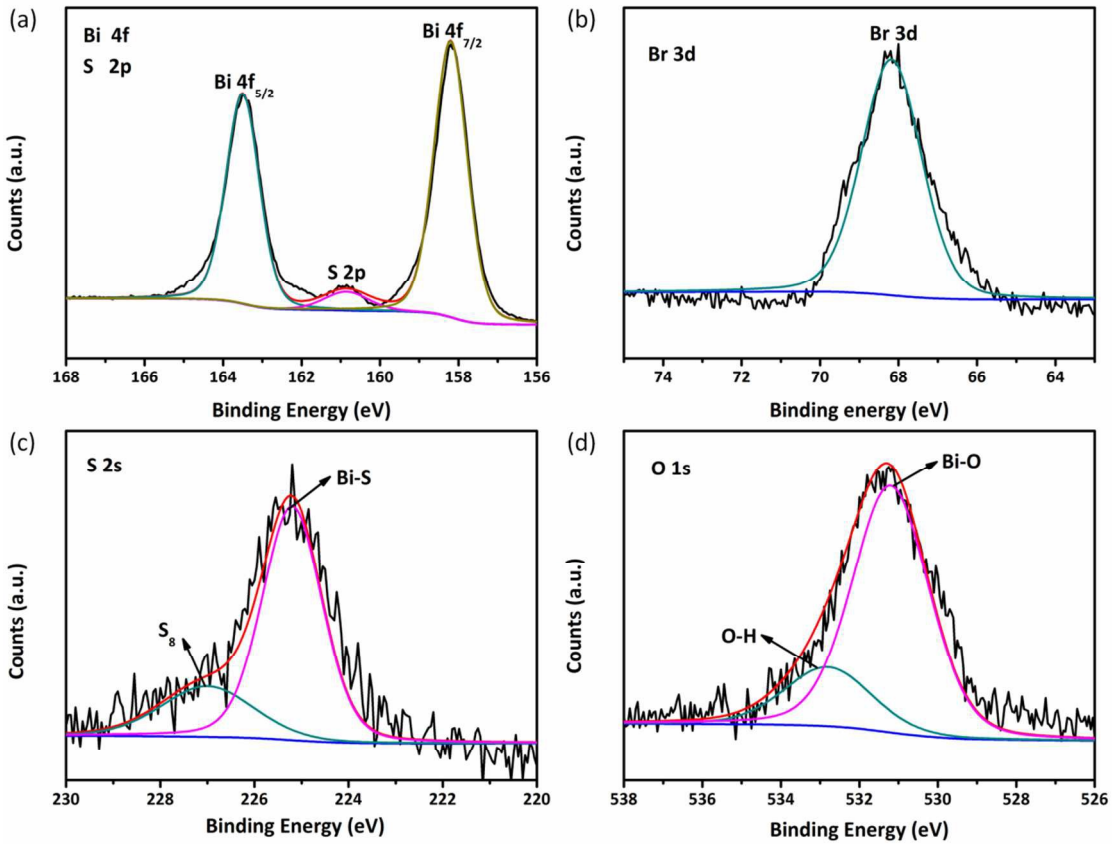

Fig. 5. XPS spectra for the hierarchical heterostructured Bi_2S_3/BiOBr sphere: (a) Bi 4f and S 2p, (b) Br 3d, (c) S 2s, and (d) O 1s.

comparison, the photocatalytic activity of P25 and the direct photolysis of RhB in the absence of the photocatalyst were also tested under the same conditions. Fig. 8a shows the concentration changes of RhB over different catalysts with the same irradiation time. The self-photolysis of RhB is negligible and the hierarchical heterostructured Bi_2S_3/BiOBr sphere exhibits the highest photocatalytic activity. The degradation efficiency achieved at 98.6% after 80 min irradiation compared with 0.8%, 36.4% and 14.7% for Bi_2S_3, BiOBr and P25, respectively. The degradation efficiency of Bi_2S_3/BiOBr is about 2.7 times higher than that of the pure BiOBr. Fig. 8b shows the temporal evolution of the absorption spectrum of RhB solution in the presence of Bi_2S_3/BiOBr sphere. The absorption peak at 553 nm decreases gradually as the irradiation time increased and completely disappeared after 80 min, indicating the destruction of the conjugated structure. And the stepwise blue shift of the main peak can be attributed to the de-ethylation of RhB, accompanied by slight concomitant blue-shifts from 554 to 492 nm of the maximum absorption. This phenomenon can be interpreted by the incomplete mineralization of RhB during the visible light irradiation. Meanwhile, the sharp decrease and fade of the RhB (Inset) within 80 min also indicate that the hierarchical heterostructured Bi_2S_3/BiOBr sphere exhibits excellent photocatalytic activity on degradation of the RhB. In view of the practical application, the photocatalyst should be chemically and optically stable after several repeated trials. As presented in Fig. 8c, there is not a clear decrease in photodegradation efficiency after four circulatory experiments, which demonstrates that the hierarchical heterostructured Bi_2S_3/BiOBr sphere has high stability and no photocorrosion occurred during the photocatalytic oxidationprocess. Furthermore, the Bi_2S_3/BiOBr sphere also exhibits superior photocatalytic efficiency in BP degradation (Fig. S4 and Fig. S5).

3.7. Photocurrent and Electrochemical impedance spectroscopy analysis

To further understand the heterojunction effect on the enhanced photocatalytic activity of the hierarchical heterostructured Bi_2S_3/BiOBr sphere, the photoinduced charge transfer property was carefully studied. The transient photocurrent response of the pure BiOBr and the hierarchical heterostructured Bi_2S_3/BiOBr sphere were recorded for several on-off cycles of visible light

Cite this: DOI: 10.1039/c0xx00000x

www.rsc.org/xxxxxx

ARTICLE TYPE

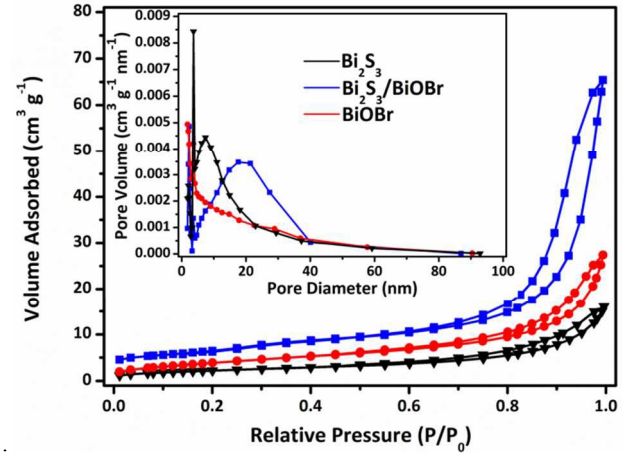

Fig. 6. Nitrogen adsorption-desorption isotherms of the pure Bi_2S_3, BiOBr, and the hierarchical heterostructured Bi_2S_3/BiOBr sphere; and the corresponding pore size distribution (inset).

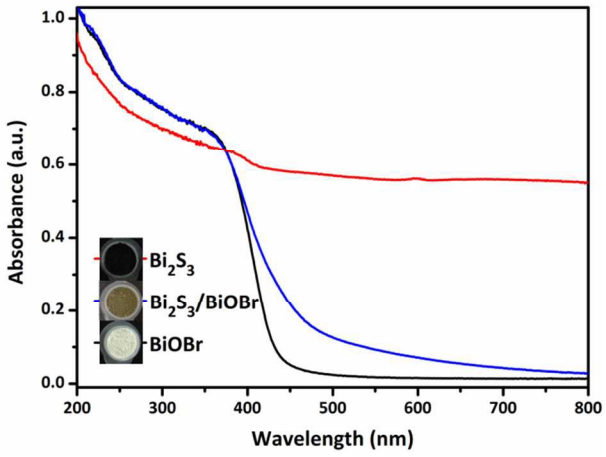

Fig. 7. UV-vis diffuse reflectance spectra of the pure Bi_2S_3, the hierarchical heterostructured Bi_2S_3/BiOBr spheres, and the pure BiOBr; the inset shows the corresponding photos of these samples.

irradiation. As can be seen from the Fig. 9a, the dark current is very low, while the current is drastically increased under irradiation, and the photocurrent comes back to the original value as soon as the illumination stopped. This result indicates that the photocurrent of the system is mostly due to the photocurrent produced by the illumination of visible light on the photoanode. Moreover, the hierarchical heterostructured Bi_2S_3/BiOBr sphere shows increased current compared with the pure BiOBr, revealing the recombination of electron-hole pairs was greatly inhibited and the separation of photogenerated charges at the interface between Bi_2S_3 and BiOBr was more effectively realized.[44] It also means that the Bi_2S_3/BiOBr heterojunction can effectively reduces the recombination rate of photogenerated electron-hole pairs, and prolongs the life time of photogenerated carriers.

Electrochemical impedance spectroscopy (EIS) curve was also employed to investigate the charge transfer resistance and the separation efficiency of photogenerated electron-hole pairs. As displayed in Fig. 9b, the diameter of the Nyquist circle of the hierarchical heterostructured Bi_2S_3/BiOBr spheres is smaller than that of BiOBr, indicating the decrease of resistance and captance, and leading to a fast interfacial charge transfer process as well as an effective separation of photogenerated electron-hole pairs.[45] Additionally, the result of the PL (Fig. S7) is also consistent with those of photocurrent response and EIS curve.

3.8. Effects of reactive species analysis

It is well known that a series of reactive species in the photocatalytic oxidation process including hydroxyl radicals(•OH), active holes (h^+) and superoxide radicals ($•O_2^-$) generated on the basis of photoinduced electrons and holes directly determine the photocatalytic performance. Therefore, the role of different reactive species was estimated by adding various scavengers and N_2 purging without adding any scavengers in the photocatalytic degradation of RhB to investigate the underlying photocatalytic mechanism in detail. In a series of experimental studies, benzoquinone (BQ),[34] *tert*-butyl alcohol (TBA)[46] and ammonium oxalate (AO)[47] are adopted as the traps for $•O_2^-$ radicals, •OH radicals and h^+, respectively. The concentration of BQ, TBA and AO in the reaction system is 10, 1.0 and 1.0 mmol L^{-1}, respectively. Compared with the result of comparison with no scavenger, the more degradation of RhB, the reactive species play more important role in the reaction. Fig. 10a shows the variation of RhB degradation with different quenchers. After the addition of BQ or AO, the photodegradation of RhB was inhibited significantly, implying that the h^+ and $•O_2^-$ radicals played major roles in the hierarchical heterostructured Bi_2S_3/BiOBr sphere system. In addition, an anaerobic experiment was carried out to investigate the effect of O_2.[46] The degradation of RhB in the presence of N_2 decreased obviously due to the reduction of active $•O_2^-$ radicals. This result reveals that O_2 act as an efficient electron trap, which is responsible for the direct generation of $•O_2^-$ radicals and restrains the recombination of electron hole pairs. Differently, the addition of TBA shows a weaker effect in photocatalytic oxidation process of RhB, indicating the •OH radicals was formed during the photocatalytic process, but did not dominate the photodegradation. The results clearly show that the h^+ and $•O_2^-$ radicals played more important roles than the •OH radicals in the photodegradation of RhB. Moreover, the photoluminescence (PL) technique with terephthalic acid (TA) as a probe molecule was introduced to further monitor the formation of •OH radicals on the surface of the photocatalysts under visible light irradiation, in which TA can readily react with •OH radicals to produce the highly fluorescent product, 2-hydroxyterephthalic acid.[48] The experimental

Cite this: DOI: 10.1039/c0xx00000x

www.rsc.org/xxxxxx

ARTICLE TYPE

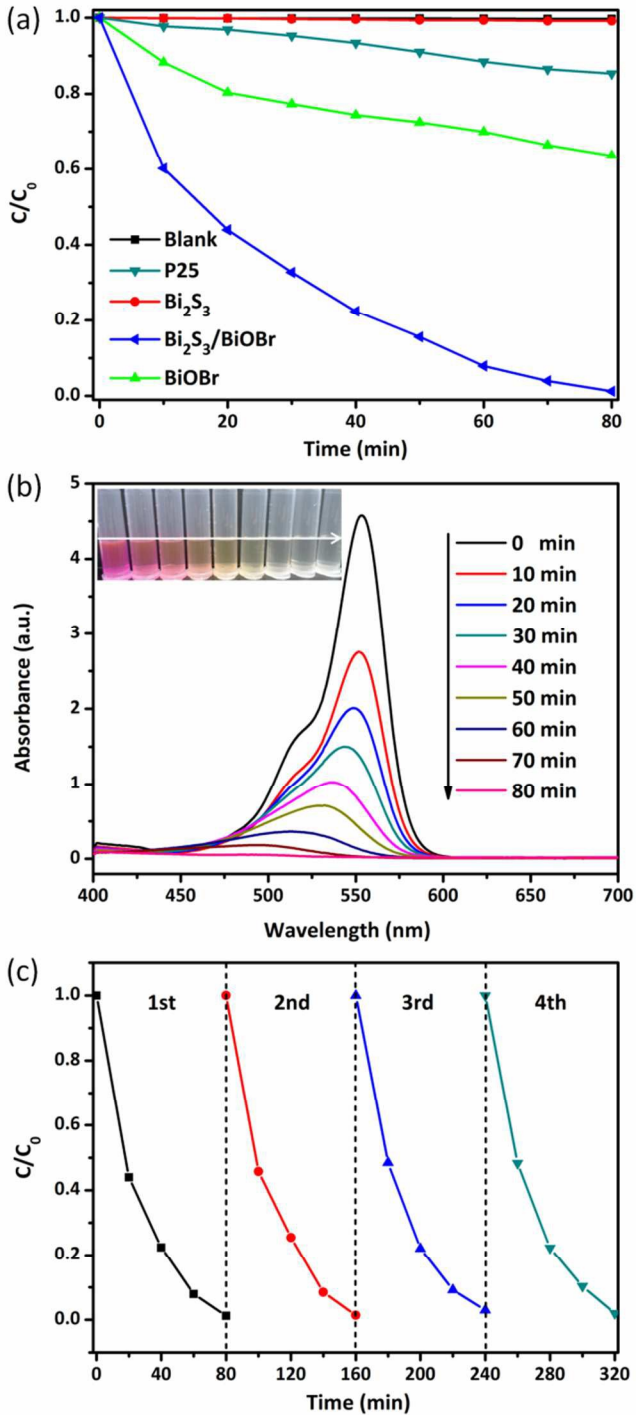

Fig. 8. (a) Comparison of photocatalytic activities of the pure Bi_2S_3, BiOBr, P25, and the hierarchical heterostructured Bi_2S_3/BiOBr spheres on the degration of RhB under visible-light irradiation ($\lambda > 420$ nm); (b) absorption changes of RhB aqueous solution in the presence of the Bi_2S_3/BiOBr composite; and (c) recycling tests on the hierarchical heterostructured Bi_2S_3/BiOBr spheres for the degradtion of RhB under visible light irradiation ($\lambda > 420$ nm).

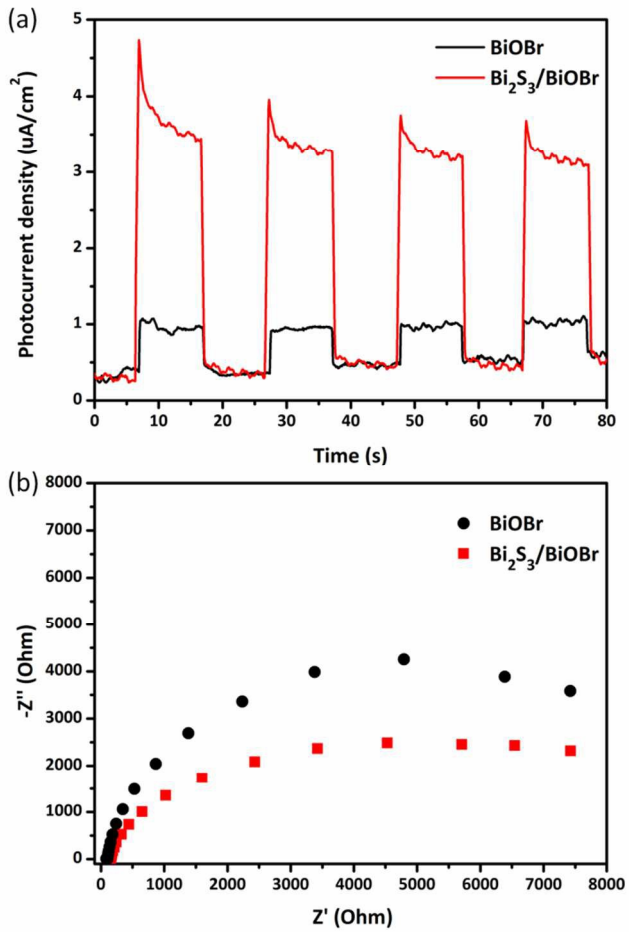

Fig. 9. (a) Transient photocurrent responses of the pure BiOBr, the hierarchical heterostructured Bi_2S_3/BiOBr sphere in 1 mol L^{-1} Na_2SO_4 aqueous solution under visible light irradiation ($\lambda > 420$ nm); and (b) the corresponding of electrochemical impedance spectroscopy.

procedure is similar as for the photocatalytic process, except that the RhB solution is replaced by a 5×10^{-4} mol L^{-1} TA solution in 2×10^{-3} mol L^{-1} NaOH solution. At regular intervals, the suspension solution was taken, centrifuged and measured on a JASCO FP-6500 type fluorescence spectrophotometer. The PL emission spectra excited at 315 nm from TA solution was measured and shown in Fig. 10b. Obviously, the PL signal at about 425 nm gradually increased as the irradiation proceeded, suggesting the generation of •OH radicals. Nevertheless, the intensity of the PL signal was comparatively weak relative to the previous report, [49] indicating that only a small amount of •OH radicals were formed. This result further confirms that the •OH radical were not the dominant reactive species. In conclusion, the h^+ and $•O^{2-}$ radicals could be considered as the main reactive species in the photocatalytic oxidation process.

Cite this: DOI: 10.1039/c0xx00000x

www.rsc.org/xxxxxx

ARTICLE TYPE

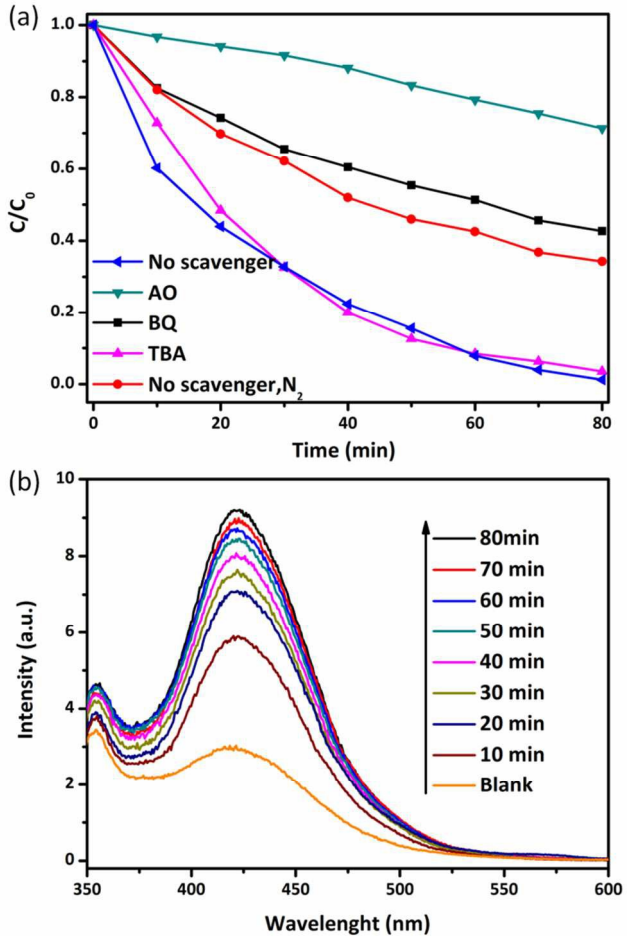

Fig. 10. (a) The effects of reactive species in the photodegradation process of RhB over Bi_2S_3/BiOBr heterostructures and (b) •OH trapping PL spectral changes over the hierarchical heterostructured Bi_2S_3/BiOBr spheres in TA solution under visible light irradiation (λ > 420 nm).

3.9. Photocatalytic mechanism

The above results reveal that the formation of heterojunction by combining BiOBr with Bi_2S_3 could obtain the enhanced photocatalytic activity, this should be attributed to the efiicient separation and fast transfer of photogenerated charges at the interface of heterojunctions.[50-53] The theoretical calculated conduction band (CB) and valence band (VB) of Bi_2S_3 is -0.76[54] and 0.54 eV, respectively, while the CB and VB of BiOBr is estimated to be 0.30[41, 52, 55, 56] and 3.15 eV, suggesting that BiOBr and Bi_2S_3 match the band potentials in BiOBr-Bi_2S_3 heterojunctions. Fig. 11 is the charge transfer pathway of the RhB degradation process over Bi_2S_3/BiOBr under visible light irradiation. Clearly, as the VB of BiOBr (3.15 eV) > the VB of Bi_2S_3 (0.54 eV) > the CB of BiOBr (0.30 eV) > the CB of Bi_2S_3 (-0.76 eV), the staggered band gap structure of Bi_2S_3/BiOBr heterojunction is favorable for the transfer of photogenerated charge carriers.[57] The photoinduced electrons can be transfered easily from the VB to the CB of Bi_2S_3 and then injected into the more positive CB of BiOBr, meanwhile the holes left on the VB top of BiOBr and moved in the opposite direction to the VB top of Bi_2S_3. It makes the charge separation more efficient and inhibits the probability of electron-hole recombination, resulting in an enhanced photocatalytic activity. Moreover, the VB potential of Bi_2S_3 (1.42 eV) is less positive than the standard reduction potential of •OH/OH^- (1.99 eV),[43] suggesting that the h^+ on the surface of Bi_2S_3 cannot oxidize OH^- into •OH radicals. Therefore, it is theoretically reasonable that the photocatalytic degradation of RhB could be attributed to the reaction with h^+ directly rather than •OH radicals. In addition, it seems that the CB potential of BiOBr (0.30 eV) is not negative enough to reduce the O_2 to the $•O_2^-$ radicals because the single-electron reduction potential of O_2 is -0.046 eV.[58] However, it impedes the formation of $•O_2^-$ radicals by photogenerated electrons from the higher levels of conduction bands. Because the electrons in the VB of Bi_2S_3 could be excited up to a higher potential edge (-2.41 eV) under visible light illumination with energy less than 2.95 eV (λ > 420 nm), while that of BiOBr could only be excited up to 0.20 eV. The reformed CB edge potential of Bi_2S_3 (-2.41 eV) is more negative than that of BiOBr (0.20 eV). As a result, part of electrons on the CB of Bi_2S_3 react with O_2 adsorbed on the interface of Bi_2S_3/BiOBr to form $•O_2^-$ radicals while transferring to the CB of BiOBr. The experiments to evaluate the role of reactive species has also demonstrates the existence of $•O_2^-$ radicals.

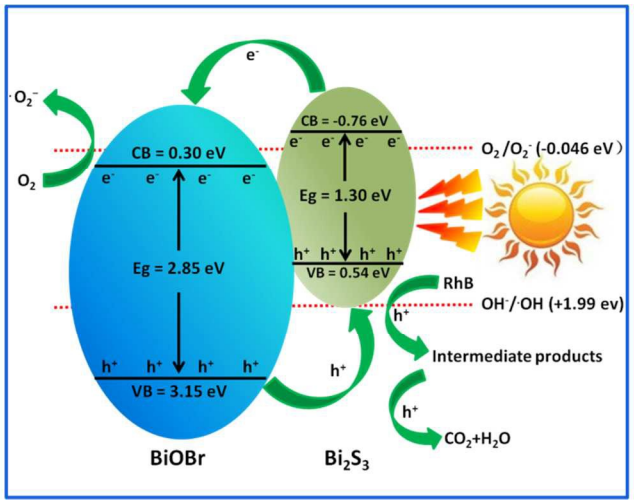

Fig. 11. Schematic diagram of electron-hole pairs separation and the possible reaction mechanism over the hierarchical heterostructured Bi_2S_3/BiOBr sphere under visible light irradiation.

4. Conclusion

In summary, we have developed a simple solvothermal approach

Cite this: DOI: 10.1039/c0xx00000x

www.rsc.org/xxxxxx

ARTICLE TYPE

to fabricate ideal hierarchical heterostructured Bi_2S_3/BiOBr spheres. The as-prepared Bi_2S_3/BiOBr spheres exhibit superior photocatalytic activity on the degradation of RhB and BP compared with the pure BiOBr under visible light irradiation, which could be mainly attributed to the formation of heterojunction in the interface of Bi_2S_3 and BiOBr. Additionally, the enlarged specific surface area played a significant role for the enhanced photocatalytic activity. The mechanism discussion demonstrates that the photocatalytic degradation of RhB and BP could facilitate the action of h^+ *via* direct hole oxidation process and the oxidation action of the generated $\bullet O_2^-$ radicals, but the •OH radicals is verified to be inappreciable in the Bi_2S_3/BiOBr photocatalysis. Such heterostructured photocatalysts may be a promising candidate for wastewater purification and environmental remediation.

Acknowledgements

The authors acknowledge the financial support of this work by Natural Science Foundations of China (Grant No. 21276104 and 21306030), the Natural Science Foundations of Guangdong Province (Grant No. s2013040015229), and the Fresh Talent Program of Guangzhou University (Grant No. 201302).

Notes and references

[a]*Department of Chemistry, Jinan University, Guangzhou 510632, China. Fax: +86 20 85226262; Tel.: +86 20 85225036; E-mail addresses: tzhangym@jnu.edu.cn (Y.-M. Zhang).*

[b]*School of Chemistry and Chemical Engineering/Guangzhou Key Laboratory for Environmentally Functional Materials and Technology, Guangzhou University, Guangzhou 510006, China. Fax: +86 20 39366908; Tel.: +86 20 39366908; E-mail addresses: lzqgzu@gzhu.edu.cn (Z.-Q. Liu).*

† Electronic Supplementary Information (ESI) available: Detailed experimental section, supporting figures and data tables. See DOI: 10.1039/b000000x/

1. M. A. Shannon, P. W. Bohn, M. Elimelech, J. G. Georgiadis, B. J. Mariñas and A. M. Mayes, *Nature*, 2008, **452**, 301-310.
2. Z. Yi , J. Ye , N. Kikugawa, T. Kako, S. Ouyang, H. S. Williams, H. Yang, J. Cao, W. Luo, Z. Li, Y. Liu and R. L. Withers, *Nat. Mater.*, 2010, **9**, 559-564.
3. J. Ran, J. Zhang, J. Yu and S. Qiao, *ChemSusChem*, 2014, 7, 3426-3434.
4. J. Zhang, J. Yu, M. Jaroniec and J. Gong, *Nano Lett.*, 2012, **12**, 4584-4589.
5. J. Zhang, L. Qi, J. Ran, J. Yu, S. Qiao, *Adv. Energy Mater.*, 2014, **4**, 1301925.
6. J. Ran, J. Zhang, J. Yu, M. Jaroniec and S. Qiao, *Chem. Soc. Rev.*, 2014, **43**, 7787-7812.
7. G. Liu, H. Yang, X. Wang, L. Cheng, J. Pan, G. Lu and H. Cheng, *J. Am. Chem. Soc.*, 2009, **131**, 12868-12869.
8. J. Zhang, Y. Wu, M. Xing, S. A. K. Leghari and S. Sajjad, *Energy Environ. Sci.*, 2010, **3**, 715-726.
9. T. Yang, L. Huang, Y. Harn, C. Lin, J. Chang, C. Wu and J. Wu, *Small*, 2013, **9**, 3169-3182.
10. J. Yu and J. Ran, *Energy Environ. Sci.*, 2011, **4**, 1364-1371.
11. J. Zhang, F. Shi, J. Lin, D. Chen, J. Gao, Z. Huang, X. Ding and C. Tang, *Chem. Mater.*, 2008, **20**, 2937-2941.
12. J. Song, C. Mao, H. Niu, Y. Shen and S. Zhang, *CrystEngComm*, 2010, **12**, 3875-3881.
13. J. Jiang, K. Zhao, X. Xiao and L. Zhang, *J. Am. Chem. Soc.*, 2012, **134**, 4473-4476.
14. S. Shenawi-Khalil, V. Uvarov, S. Fronton, I. Popov and Y. Sasson, *J. Phys. Chem. C*, 2012, **116**, 11004-11012.
15. J. Xiong, Q. Dong, T. Wang, Z. Jiao, G. Lu and Y. Bi, *RSC Adv.*, 2014, **4**, 583-586.
16. Y. Fang, Y. Huang, J. Yang, P. Wang and G. Cheng, *Environ. Sci. Technol.*, 2011, **45**, 1593-1600.
17. D. Zhang, J. Li, Q. Wang and Q. Wu, *J. Mater. Chem. A*, 2013, **1**, 8622-8629.
18. W. Lin, X. Wang, Y. Wang, J. Zhang, Z. Lin, B. Zhang and F. Huang, *Chem. Commun.*, 2014, DOI: 10.1039/C3CC41498A.
19. G. Jiang, R. Wang, X. Wang, X. Xi, R. Hu, Y. Zhou, S. Wang, T. Wang and W. Chen, *ACS Appl. Mater. Interfaces*, 2012, **4**, 4440-4444.
20. G. Jiang, X. Wang, Z. Wei, X. Li, X. Xi, R. Hu, B. Tang, R. Wang, S. Wang, T. Wang and W. Chen, *J. Mater. Chem. A*, 2013, **1**, 2406-2410.
21. Z. Ai, W. Ho and S. Lee, *J. Phys. Chem. C*, 2011, **115**, 25330-25337.
22. J. Fu, Y. Tian, B. Chang, F. Xi and X. Dong, *J. Mater. Chem.*, 2012, **22**, 21159-21166.
23. X. Wei , C. Chen, S. Guo, F. Guo, X. Li, X. Wang, H. Cui, L. Zhao and W. Li, *J. Mater. Chem. A*, 2014, **2**, 4667-4675.
24. L. Kong, Z. Jiang, T. Xiao, L. Lu, M. Jones and P. Edwards, *Chem. Commun.*, 2011, **47**, 5512-5514.
25. Y. Li, Y. Liu, J. Wang, E. Uchaker, Q. Zhang, S. Sun, Y. Huang, J. Li and G. Cao, *J. Mater. Chem. A*, 2013, **1**, 7949-7956.
26. L. Ye, J. Liu, C. Gong, L. Tian, T. Peng and L. Zan, *ACS Catal.*, 2012, **2**, 1677-1683.
27. L. Cademartiri, F. Scotognella, P. G. O'Brien, B. V. Lotsch, J. Thomson, S. Petrov, N. P. Kherani and G. A. Ozin, *Nano Lett.*, 2009, **9**, 1482-1486.
28. Z. Ge, B. Zhang, P. Shang and J. Li, *J. Mater. Chem.*, 2011, **21**, 9194-9200.
29. H. Liao, M. Wu, M. Jao, C. Chuang, Y. Chen and W. Su, *CrystEngComm*, 2012, **14**, 3645-3652.
30. A. A. Tahir, M. A. Ehsan, M. Mazhar, K. G. U. Wijayantha, M. Zeller and A. D. Hunter, *Chem. Mater.*, 2010, **22**, 5084-5092.
31. H. Yu, J. Huang, H. Zhang, Q. Zhao and X. Zhong, *Nanotechnology*, 2014, **25**, 215702.
32. S. Luo, F. Chai, L. Zhang, C. Wang, L. Li, X. Liu and Z. Su, *J. Mater. Chem.*, 2012, **22**, 4832-4836.
33. D. Ma, M. Guan, S. Liu, Y. Zhang, C. Zhang, Y. He and S. Huang, *Dalton Trans.*, 2012, **41**, 5581-5586.
34. J. Cao, B. Xu, H. Lin, B. Luo and S. Chen, *Dalton Trans.*, 2012, **41**, 11482-11490.
35. H. Cheng, B. Huang, X. Qin, X. Zhang and Y. Dai, *Chem. Commun.*, 2012, **48**, 97-99.
36. Z.-Q. Liu, W.-Y. Huang, Y.-M. Zhang and Y.-X. Tong, *CrystEngComm.*, 2012, **14**, 8261-8267.
37. J. Xu, L. Li, C. Guo, Y. Zhang and W. Meng, *Appl. Catal. B: Environ.*, 2013, **130**, 285-292.
38. X. X. Wei, H. Cui, S. Guo, L. Zhao, W. Li, *J. Hazard. Mater.*, 2013, **263**, 650– 658.
39. D. Zingg and D. Hercules, *J. Phys. Chem.*, 1978, **82**, 1922-1995.

40. L. Kong, Z. Jiang, H. Lai, R. J. Nicholls, T. Xiao, M. O. Jones and P. P. Edwards, *J. Catal*., 2012, **293**, 116-125.
41. F. Li, Q. Wang, J. Ran, Y. Hao, X. Wang, D. Zhao and S. Qiao, *Nanoscale*, 2015, **7**, 1116-1126.
42. J. Zhang, S. Liu, J. Yu and M. Jaroniec, *J. Mater. Chem.*, 2011, **21**, 14655-14662.
43. L. Kong, Z. Jiang, T. Xiao, L. Lu, M.O. Jones and P. P. Edwards, *Chem. Commun.*, 2011, **47**, 5512–5514.
44. S. Zhang, J. Li, M. Zeng, G. Zhao, J. Xu, W. Hu, and X. Wang, *ACS Appl. Mater. Interfaces.*, 2013, **5**, 12735−12743.
45. J. X. Xia, J. Di, S. Yin, H. Xu, J. Zhang, Y.G. Xu, L. Xu, H.M. Li and M.X. Ji, *RSC Adv*., 2014, **4**, 82.
46. Y. Li, J. Wang, H. Yao, L. Dang and Z. Li, *J. Mol. Catal. A:Chem.*, 2011, **334**, 116.
47. N. Zhang, S. Liu, X. Fu and Y. Xu, *J. Phys. Chem. C*, 2011, **115**, 9136.
48. J. Cao, X. Li, H. Lin, S. Chen, and X. Fu, *J. Hazard. Mater.*, 2012, **239**,316-324.
49. L. Li, L. Ai, C. Zhang, and J. Jiang, *Nanoscale*, 2014, **6**, 4627-4634.
50. C. Pan, J. Xu, Y. Wang, D. Li and Y. Zhu, *Adv. Funct. Mater.*, 2012, **22**, 1518-1524.
51. Q. Xiang, J. Yu and M. Jaroniec, *J. Am. Chem. Soc.*, 2012, **134,** 6575-6578.
52. J. Fu, Y. Tian, B. Chang, F. Xi and X. Dong, *J. Mater. Chem.*, 2012, **22**, 21159-21166.
53. X. Li, J.G. Yu, J. Low, Y. Fang, J. Xiao and X. Chen, *J. Mater. Chem. A*, 2015, DOI: 10.1039/c4ta04461d
54. Y. Bessekhouad, D. Robert, and J.V. Weber, *J Photoch Photobio A*, 2004, **163**, 569–580
55. R. Yuan, S. Fan, H. Zhou, Z. Ding, S. Lin, Z. Li, Z. Zhang, C. Xu, L. Wu, X. Wang, and X. Fu, *Angew. Chem. Int. Ed.*, 2013, **52**, 1035-1039
56. W. Zhang, Q. Zhang, and F. Dong, *Ind. Eng. Chem. Res.*, 2013, **52**, 6740-6746
57. H. Cheng, B. Huang and Y. Dai, *Nanoscale*, 2014, **6**, 2009-2026.
58. J. Cao, B. Xu, B. Luo, H. Lin, and S. Chen, *Catal. Commun.*, 2011, **13**, 63-68.